UNRESTRAINED MEASUREMENT OF ARM MOTION BASED ON A WEARABLE WIRELESS SENSOR NETWORK

[1]SREENIVASULU & [2]N.SUBBARAO
[1,2]ECE Department,Quba Engineering College Nellore (Dist.), Andhra Pradesh,
Email:sreenivasulu.samadhi@gmail.com, nsr.rao@gmail.com, faruq_sk2003@gmail.com

Abstract—Techniques that could precisely monitor human motion are useful in applications such as rehabilitation, virtual reality, sports science, and surveillance. Most of the existing systems require wiring that restrains the natural movement. To overcome this limitation, a wearable wireless sensor network using accelerometers has been developed in this paper to determine the arm motion in the sagittal plane. The system provides unrestrained movements and improves its usability. The lightweight and compact size of the developed sensor node makes its attachment to the limb easy. Experimental results have shown that the system has good accuracy and response rate when compared with a goniometer.

Index Terms—*Human body motion, rehabilitation, wearable sensor, wireless sensor network.*

I. INTRODUCTION

TRACKING of human motion has attracted significant interest in recent years due to its wide-ranging application such as rehabilitation [1], virtual reality [2], [3], sports science [4], and surveillance [5]. Existing methods include mechanical, visual, audio, radar, magnetic, and inertial tracking [6]. Visual tracking involves the use of a single or multiple cameras. The captured images suffer from problems due to occlusion, lighting changes, clutter, shadow, and noise [5], [7]. Single-camera tracking is normally based on model, contour, or feature, but it easily generates ambiguity due to occlusion or depth. Multiple cameras can reduce the ambiguity and handle occlusion but are costly.

In recent years, inertial and magnetic tracking [8]–[12] have attracted much interest as they are source-free approaches unlike the audio and radar that require an emission source. The development of microelectromechanical system technology has also made such sensors lighter, smaller, and cheaper. Consequently, they are good candidates for an ambulatory measurement system used in telerehabiliation [13], [14] conducted in the patient's home or office. This will also greatly reduce the frequency to visit the hospital for patients undergoing physiotherapy. A good ambulatory system has to meet several design criteria, such as lightweight, easy attachment, little hindrance to natural movement, capability for long-term monitoring, high accuracy, and ideally low latency. Research work has also been conducted to make such system portable [15], [16] and wearable [17]–[20]. However, existing systems have many wiring and thus pose a constraint on the body movement. In this paper, a wearable wireless sensor system is proposed to overcome this limitation. The wireless feature enables the unrestrained motion of the human body as opposed to a wired monitoring device and makes the system truly portable. This will also allow the system to be deployed in a cluttered home environment. The small form factor and lightweight feature of the sensor nodes also allow easy attachment to the limbs. The autonomous computing capability of each sensor node will also allow for distributed control architecture to be implemented. Such a system is also lower in cost compared with a sophisticated visual tracking system with multiple tracking cameras. The low power consumption of each sensor node will also allow for long-term monitoring.

The organization of this paper is as follows: Section II describes the configuration of the prototype system. This is followed by the measurement approach in Section III. The error modeling of the tilt measurement is investigated in Section IV. Calibration for the sensor node is presented in Section V. Section VI presents the results from the experiments conducted. The system performance in terms of accuracy and latency has been evaluated. Finally, we conclude this paper in Section VII.

II. SYSTEM CONFIGURATION

Fig. 1 shows the configuration of the system. It is observed that the system consists of a number of sensor nodes that wirelessly communicate to a central coordinator in a star network topology. The coordinator is in turn connected to a PC via an RS232 wired link. Fig. 2 shows the coordinator with a PIC18LF2620 microcontroller. The coordinator may use either a mains power or a 9-V rechargeable battery.

Fig. 3 shows the picture of a sensor node. Each sensor node is equipped with a capacitive micromachined accelerometer (Freescale MMA7261QT) that can be used to detect tilt angle of up to three axes. The sensor nodes are attached to the human limbs and operate completely untethered. They are powered by a 6-V alkaline battery. The developed sensor node has a small form factor measuring 40 × 39 × 16 mm. It weighs only 19 g without battery. The battery will add another 14 g to the system.

For this system, the MiWi network protocol [21] is

used due to its small stack. It is based on the medium-access control and physical layers of the IEEE 802.15.4 specification for low-rate wireless personal area networks. A detail discussion on the

Fig.1.Generalconfigurationofthesystem.

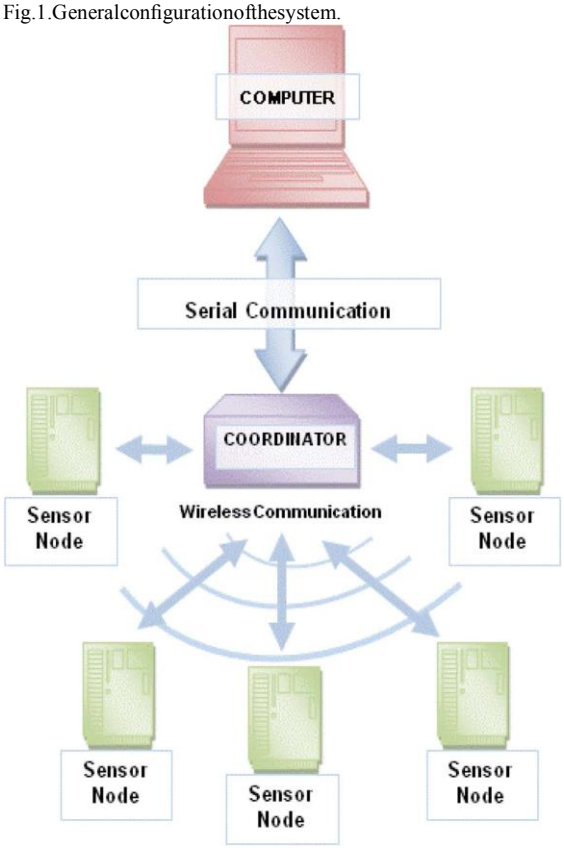

Fig.2.Photographofanetworkcoordinator.

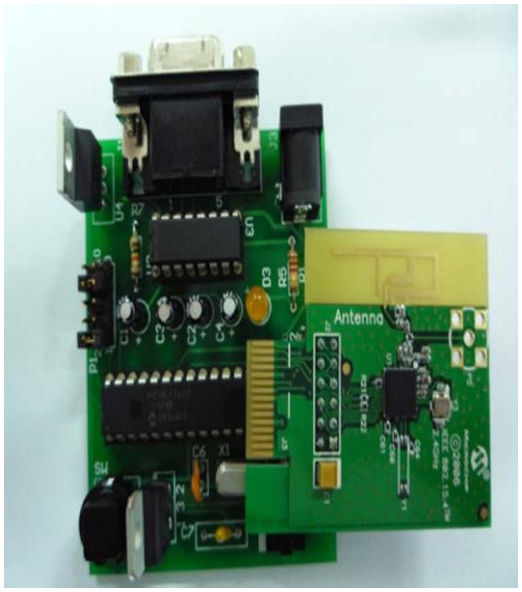

Fig.3.Photographsofasensornode.(a)Frontview,withamicrocontrollerunitandanaccelerometer.(b)Backview,withamicrochipRFmodule.

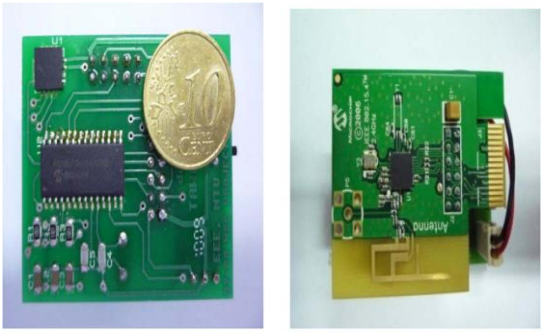

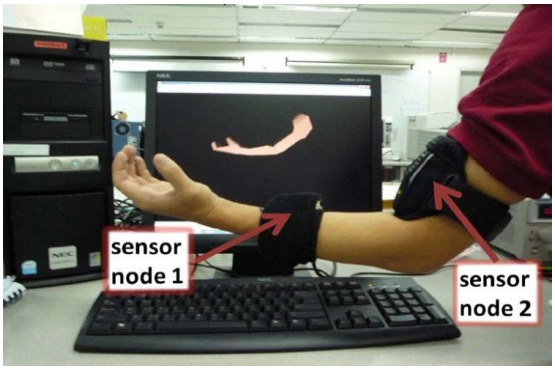

Fig. 4. Attachment of the sensor nodes on the human arm.

choice of wireless standard, protocol, and the implementation of the wireless platform is given in [22]. During operation, the accelerometer on each sensor node will measure the three-axis (XY Z) acceleration. These measurements are then digitized via the analog-to-digital converter (ADC) module of the microcontroller and wirelessly transmitted using the RF transceiver to the network coordinator. The sampling rate for the ADC is configurable and is set to 10 Hz for a two-sensor node network system. The coordinator subsequently transfers the data to the PC via an RS232 interface at a baud rate of 19 200 bits/s for algorithmic computation and motion rendering. The PC used in the experiments runs on a Pentium 4 640 CPU with a clock speed of 3.2 GHz. The MATLAB virtual reality toolbox is used for the motion rendering.

III. MEASUREMENT APPROACH

Fig. 4 shows the attachment of the sensor nodes to the upper arm and the forearm. The figure also shows the corresponding movements of the arm rendered in a virtual reality environment on the computer screen.

In this paper, we investigate the movement of the human arm along sagittal plane, i.e., the plane that bisects the human body into left and right [23]. This corresponds to the flexion and extension movements of the forearm and the upper arm. Flexion is a bending movement in which the relative angle of the joint between the adjacent segments decreases. Extension is a straightening movement in which the relative angle of the joint between two adjacent

segment increases as the joint returns to the reference anatomical position. For the physical therapist, the range of the elbow motion and shoulder joint of the patient is of particular interest for monitoring the rehabilitation progress. To capture the arm's rotational motion, an accelerometer is integrated to the sensor node as an inclinometer. An accelerometer, in general, can be used to measure the arm motion that is in static and dynamic conditions. The details are described in the following sections.

A. Tilt/Static Measurement

Fig. 5 shows an accelerometer mounted on the forearm. In the static conditions, i.e., the arm is not moving, the tilt angle θ of the accelerometer can be determined by measuring the acceleration due to gravity g, as shown in Fig. 5.

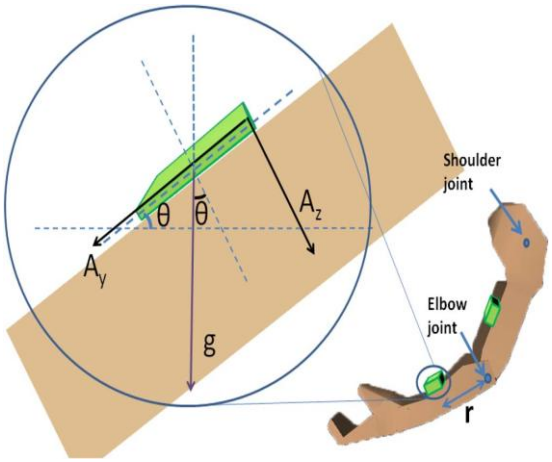

Fig. 5. Tilt-angle measurement in the Y −Z plane. From Fig. 5,

$$\theta = \tan^{-1}\frac{A_Y}{A_Z} \quad (6)$$

rotation. Rearranging (9) and (10), we have

$$A_Y(t) = g\sin\theta - r\left(\frac{d\theta}{dt}\right)^2 \quad (11)$$

$$A_Z(t) = g\cos\theta + r\frac{d^2\theta}{dt^2}. \quad (12)$$

the Z-axis that are due to gravity can be determin

$$\left(\frac{\lambda_Z - \lambda_{Z_o}}{\lambda_Y - \lambda_{Y_o}}\right)$$

) where λ_Y and λ_Z are the ADC output values of the accelerometer in the Y -and Z-axes, respectively, and λ_{Y_o} and λ_{Z_o} are the offsets of the accelerometer at 0g.

B. Dynamic Measurement

In the dynamic condition, modeling the rotation of the accelerometer in a circular motion yields

$a_Y = g\sin\theta - A_Y(t)$ (7) $a_Z = A_Z(t) - g\cos\theta$ (8)

where a_Y and a_Z are the accelerations in the Y -and Z-axes of the accelerometer.

In terms of derivatives of θ,wehave

$$r\left(\frac{d\theta}{dt}\right)^2 = g\sin\theta - A_Y(t) \quad (9)$$

$$r\frac{d^2\theta}{dt^2} = A_Z(t) - g\cos\theta \quad (10)$$

where r is the distance of the accelerometer from the axis of

From (11) and (12), it is observed that the value of $A_Y(t)$ is affected by the angular velocity, whereas the value of $A_Z(t)$ is affected by the angular acceleration. Equations (11) and (12) are nonlinear in nature, and a solution is nontrivial. Since the target application of this paper is rehabilitation, the angular acceleration and velocity of the human arm motion are generally small. The maximum angular velocity of the arm for a patient undergoing rehabilitation is about 10°/s or 0.17 rad/s [24]. For the angular acceleration, it is typically less than 1 rad/s [25] for most of the time during arm flexion and extension motion. This translates to an additional acceleration of 0.0043 m/s^2 in the Y -axis and 0.15 m/s^2 in the Z-axis with r =0.15 m, which is much less than the acceleration due to gravity (9.81 m/s^2). In addition, it is observed that the derivative terms are also multiplied by r. This

$$A_Y(t) = g\sin\theta - r\left(\frac{d\theta}{dt}\right)^2 \quad (11)$$

$$A_Z(t) = g\cos\theta + r\frac{d^2\theta}{dt^2}. \quad (12)$$

the accelerations A_Y in the Y -axis and A_Z in

$$\theta = \tan^{-1}\frac{A_Y}{A_Z}. \quad (3)$$

The quadrant of θ can be determined by the sign of A_Y.

The output voltage V_{out} of the accelerometer is related to the acceleration A_i of a particular axis (i = Y or Z)bythe following relationship:

$$V_{out} = V_{offset} + S \times A_i \quad (4)$$

where $S = \Delta V/\Delta g$ is the sensitivity of the accelerometer (in volts per meter per second squared), and V_{offset} is the offset of the accelerometer at 0g.

The corresponding ADC value can be expressed as

$$\lambda_i = Q\left(\frac{2^n}{V_{REF}^+ - V_{REF}^-}V_{out}\right) \quad (5)$$

where n is the resolution bits of the ADC (n =8 in this case), V_{REF}^+ and V_{REF}^- are the reference voltage levels, and Q[] is the quantizer function. The accelerometer is ratiometric, i.e., the output voltage and sensitivity linearly scale with the reference voltage. From (4) and (5), it is observed that the supply induced errors are cancelled in the analog-to-digital conversion process.

Substituting V_{out} from (4) into (5), the acceleration A_i is approximately proportional to λ_i after subtracting an equivalent ADC offset. As such, (3) can be rewritten as follows:

$$\theta = \tan^{-1}\left(\frac{\lambda_Y - \lambda_{Y_o}}{\lambda_Z - \lambda_{Z_o}}\right)$$

suggests that the effects of the additional derivative terms can be minimized by placing the sensor close to the center of rotation. Hence, the derivative terms can be neglected when determining the tilt angle. The error due to this assumption will be determined through experiments in Section VI by subjecting the sensor to varying angular rates of rotation.

C. Latency Measurement

In addition to measurement accuracy, another important performance metric is latency. Latency is the time between a motion is made and captured. In an ideal tracking system, the mean time delay after a motion is initiated until the corresponding data are transmitted should be less than 1 ms [6]. Moreover, the latency between the initiation of motion and the motion rendering should be less than 100 ms to avoid degradation of performance [26]. Thus, one of the challenges of the proposed wireless tracking system is to ensure acceptable latency when multiple sensor nodes are in use.

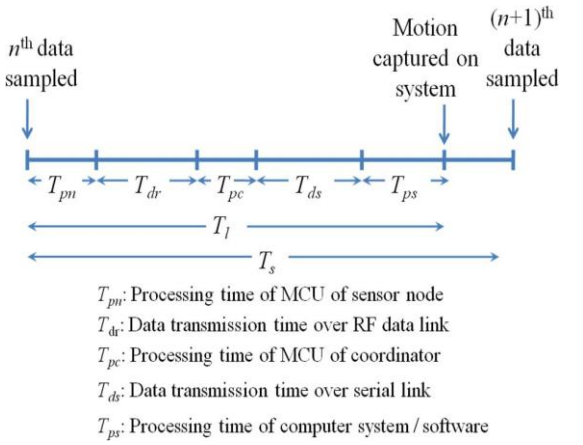

Fig.6.Latenciesinvolvedinthesampleprocessingofreal-timemotio tracking(singlenode).

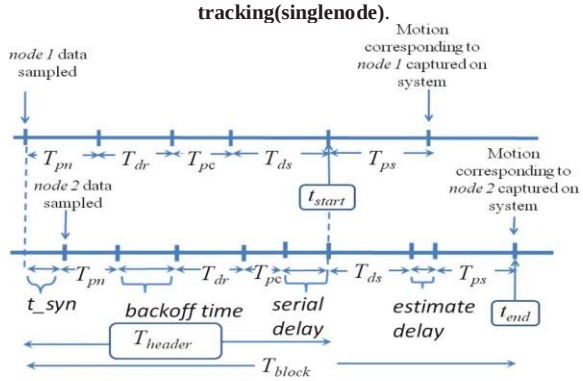

Fig. 7. Latencies involved with two sensor nodes.

Fig. 6 shows the time components contributing to the latency of the system with one sensor node. The sampling interval T_s should be greater than the sum of the total latencies T_l. Thus, the latency of the system limits its maximum sampling rate. Given that the frequency spectrum of human body motion ranges from 2 to 20 Hz [27], the sampling rate of the system should ideally be greater than 40 Hz. However, for the case of arm flexion and extension motion, the fast Fourier transform of the accelerometer signal mounted on a forearm undergoing normal and very fast flexion and extension motion shows that the majority of the frequency components fall under 1.0 Hz. Thus, an oversampling frequency at 10 Hz is more than sufficient. From Fig. 6, we have

$T_s \geq T_l = T_{pn} + T_{dr} + T_{pc} + T_{ds} + T_{ps}$. (13)

Fig. 7 shows the latency of a network with two sensor nodes and one coordinator. With multiple nodes, the figure shows that there are additional delays such as the time difference between different sensor measurements (t_syn), backoff time, serial and estimate (delay), etc. In this case, the sampling rate has to be greater than the latency of the system, i.e.,

$T_s \geq T_{block}$. (14)

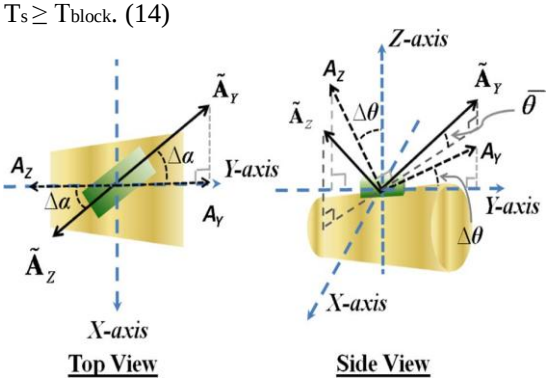

Fig. 8. Mounting errors of an accelerometer on a cylindrical limb model.

IV. ERROR MODELING

In this section, the error of the tilt measurement due to misalignment in attaching the sensor node onto the limb is investigated. The limb can be modeled as a cylindrical object with different base radii on both ends of the cylinder, as shown in Fig. 8.

From the top view of Fig. 8, it is observed that there is an error in mounting the sensor laterally. Consequently, the Y -axis of the accelerometer may not lie in the Y −Z plane. Instead, it is inclined at an angle of Δα to the Y −Z plane along the X−Y plane. A_Y is the measured acceleration of the Y -axis of the accelerometer and is related to A_Y, which the projection of A_Y onto the reference Y −Z plane by

$$A_Y = A_Y \cos\theta \cos\Delta\alpha + \sin^2\theta \quad (15)$$

where the angle θ is the angle between the Y -axis of the accelerometer and the reference X−Y plane. The mea

rotation. Rearranging (9) and (10), we have

$$A_Y(t) = g \sin\theta - r(d\theta/dt)^2$$

$$A_Z(t) = g\cos\theta + r\, d^2\theta/dt^2.$$

the Z-axis that are due to gravity can be deter

Similarly, we have the following relationships for the Z-axis of the accelerometer:

$$A_Z = g\cos\theta \quad (17)$$

J ()$_2$

$A_Z = A_z \sin\theta \cos\Delta\alpha + \cos^2\theta$. (18)

From the side view in Fig. 8, it is observed that, as a result of the sloping surface of the arm model, there is a misalignment of A_Y with respect to the reference Y -axis. As such, the tilt angle

$\hat{\theta}$ from the reference Y -axis about the X-axis is related to the true tilt angle θ from the arm by

$\hat{\theta} = \theta + \Delta\theta$ (19)

where Δθ represents the angle between A_Y at 0g and the reference Y -axis. Hence, the true tilt angle θ can be related to $\hat{\theta}$, Δθ, and Δα as

$\tan\hat{\theta} = \tan(\theta + \Delta\theta)\cos\Delta\alpha$. (20)

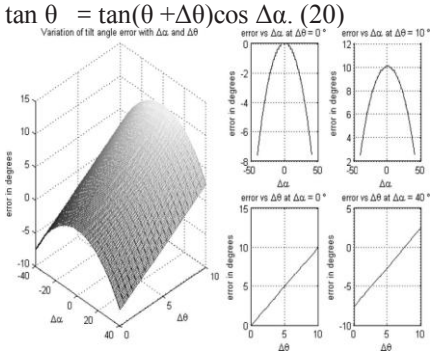

Fig. 9. Variation of tilt-angle error with Δα and Δθ.

From (20), θ approximates to θ if Δθ and Δα are small. The measured ADC values are given by

$\lambda_Y = QS_A g \sin\theta + \lambda_{Yo}$ (21)

$\lambda_Z = QS_A g \cos\theta + \lambda_{Zo}$ (22)

where $S_A = (2^n/(V_{REF}^+ - V_{REF}^-))S$.

Therefore, the measured tilt angle can be modeled as

$\hat{\theta} = \tan^{-1}\dfrac{\lambda_Y - \lambda_{Yo}}{\lambda_Z - \lambda_{Zo}}$ (23)

where $\hat{\lambda}_{Yo}$ and $\hat{\lambda}_{Zo}$ are the estimates of the 0g offset. Using (20)–(23), the tilt-angle error $\hat{\theta} - \theta$ versus the variation in the values of Δθ and Δα is shown in Fig. 9. The range of value for Δθ is from 0° to 10°, and Δα is from −40° to 40°

for an arbitrary value of θ =45°.

The graph on the left of Fig. 9 shows the error plot with variation in Δθ and Δα. The subplots on the right shows the error w.r.t. Δα with fixed values Δθ =0° and 10°,aswellas the error w.r.t. Δθ with fixed values Δα =0° and 40°.

From the plots, it is observed that the error is very close to the value of Δθ at Δα =0for fixed Δθ. The error decreases as the absolute value of Δα increases, showing a parabolic curve centered at Δα =0. The absolute value of the error ranges from 0° at Δα =0° to about 8° at Δα =40°.

For a fixed value of Δα, the error is minimum at Δθ =0. The error then linearly increases as Δθ increases. It is observed that the range of absolute value of the error is close to the range of value of Δθ, whereas the value of the error is dependent on the value of Δα. The combined effect of Δθ and Δα on the error produces the single-sheet paraboloid centered at the plane Δα =0, as shown in the 3-D plot. The results of these curves show the effect of the attachment errors on the tilt-angle determination.

V. CALIBRATION

To improve the measurement accuracy, calibration is required to obtain the 0g offset values (λ_{Yo} and λ_{Zo}) for each accelerometer. One approach is to determine the ADC output when the accelerometer is at the 0g position or when it is positioned completely level. However, such measurement is difficult and is prone to error due to mounting or orientation as discussed in Section IV. Calibration in 0g can be conducted by recording the ADC values during free fall. However, inaccuracies could arise due to unwanted rotation of the device during free fall.

Fig. 10. Mounting of a sensor node on a high-precision rotary motor for determination of angular displacement.

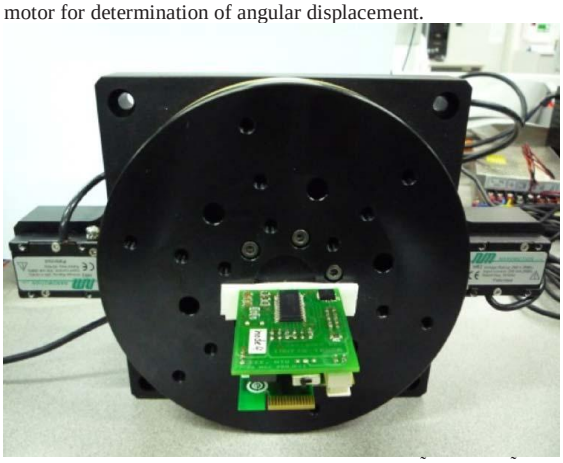

From the sinusoidal relationship of λ_Y and λ_Z with respect to the tilt angle θ as in (21) and (22), it is observed that an estimate of λ_{Yo} and λ_{Zo} can be determined by taking the mean value of λ_Y and λ_Z over a 360° cycle, in which the mounting or orientation error Δθ and Δα is cancelled out in the averaging process. This method yields more accurate result and requires no reference acceleration position that is difficult to determine in practice.

For our calibration process, the sensor node is mounted on a rotary stage, as shown in Fig. 10. The rotary stage uses two ceramic motors. It has a resolution of 0.0001° and a maximum allowable velocity of 250 mm/s. Fig. 11 shows the ADC values of the Y -and Z-axes of an accelerometer from 0° to 360° with astepsizeof5°.

From the figure, it is observed that the ADC value for the Y -and Z-axes follows sine and cosine waves as in (21) and (22), respectively. The corresponding

estimated 0g offsets $\hat{\lambda}_{Yo}$ and $\hat{\lambda}_{Zo}$ are determined to be 127.8889 and 125.9306, respectively. This calibration can then be repeated for other accelerometers attached to the other limbs.

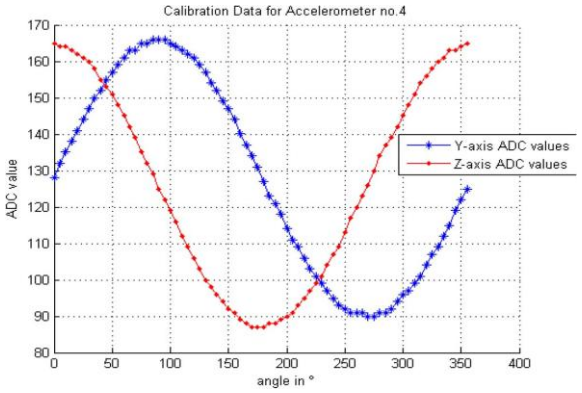

Fig.11.Calibrationdataforatypicalaccelerometer.

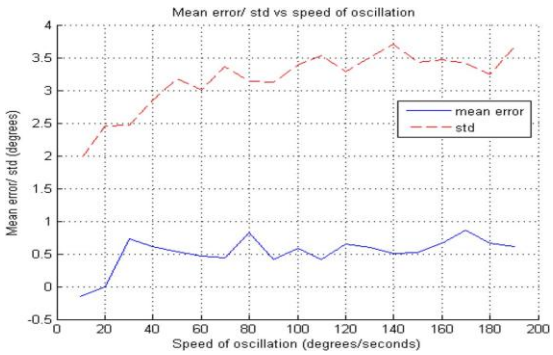

Fig. 12. Mean error and variance of accelerometer readings at various speeds.

VI. EXPERIMENTAL RESULTS

A. Accuracy

To investigate the accuracy of the proposed approach, the sensor node is first mounted on a rotary stage, as shown in Fig. 10. The stage is programmed to produce a swinging motion between ±90° with an angular speed varied from 10°/sto 190°/s. The ADC accelerometer reading with respect to time is then captured. Fig. 12 shows the mean error and variances of the angle of rotation. From the experimental results, it can be observed that the mean error is close to 0° at very low speeds of oscillation (≤ 20°/s). The mean error then fluctuates between 0.5° and 1.0° for increasing speeds of oscillation. The standard deviation, on the other hand, shows an increasing trend from

TABLE I LATENCIES ASSOCIATED WITH A SINGLE SENSOR NODE

	T_{pn}	T_{pc}	T_{ps}	T_{ds}	T_{dr}	T_l
mean time (μs)	107	90	3981	6250	1312	11028

2° to 3.7°. This is due to the effect of neglecting the additional acceleration term, apart from the gravity in (11) and (12). From this test, it is concluded that an accuracy value of 0.52° is achievable.

B. Latency of the Sensor Node

To estimate the latency of the system, 10 000 data samples have been collected from an experiment based on one sensor node with one coordinator. As shown earlier in Fig. 6, the latencies to be considered are the processing time of the sensor node T_{pn}, the processing time of the coordinator T_{pc}, and the processing time of the computer T_{ps} in determining the rotation angle. These latency times can be determined using the timer module of the microcontroller and the CPU clock in the PC. The data transmission time of the RF data link T_{dr} and the data transmission time over the serial link T_{ds} can be calculated using the RF data and serial link baud rates. For this system, the data and baud rates are 250 and 19.2 kb/s, respectively. The data propagation time over air can be ignored since the RF signal is transmitting at 3×10^8 m/s, and the time over the typical distances (10–50 m) is insignificant. The mean total latency time T_l obtained from this experiment is shown in Table I.

From Table I, the processing time of the PC is much greater than the coordinator and the sensor node. The major latency contributing to the system comes from the serial link. Thus, the total latency can be improved by employing a faster serial baud rate. A test on the system shows that the maximum supported baud rate is 57 600 bits/s, which can give us a much improved total latency T_l of 2.083 ms.

Next, we investigate the latency of the system with multiple sensor nodes. The wireless system deployed here is a non-beacon multiaccess network. Hence, all the nodes have equal access to the communication medium. Moreover, the nodes are allowed to transmit at any time as long as the channel is idle. Each sensor employs a carrier-sense multiple access with collision avoidance protocol to avoid wasteful collisions when multiple simultaneous transmissions might occur.

To determine the latency of the network with multiple sensor nodes attached to the arm, we make use of the analysis in Fig. 7, which shows the case for two sensor nodes. Fig. 7 shows that the latency T_{block} is just equivalent to the sum of $(t_{end} - t_{start}) + T_{header}$. T_{start} and t_{end} can be determined using the CPU clock in software, whereas T_{header} can be obtained from the sum of T_{pn}, T_{dr}, T_{pc}, and T_{ds} as in the case for a single sensor node. The latency for three or more sensor nodes can be determined in a similar manner. One thousand block data samples are taken for each network with up to ten sensor nodes in a star network configuration. The result from this experiment is shown in Fig. 13. From the figure, it is observed that the latency increases by about 20–40 ms with an addition of one sensor node to the existing network. From (14), the latency of the system must be less than the sampling period to meet the processing requirements. Thus, a sampling rate of 10 Hz is chosen for our two-sensor-node single-arm network. The 50-to 90-ms latency for a two-to four-sensor-node network is within the acceptable latency of 100 ms for a virtual-reality-based tracking system. There are several ways to improve the latency performance such as the use of a more advanced data collision avoidance algorithm with less time delay or the use of pipelining, leading to a more efficient computation of data. These are some possible scopes that we will investigate in future

work.

Fig. 14. Attachment of the sensor nodes and goniometer to a human arm.

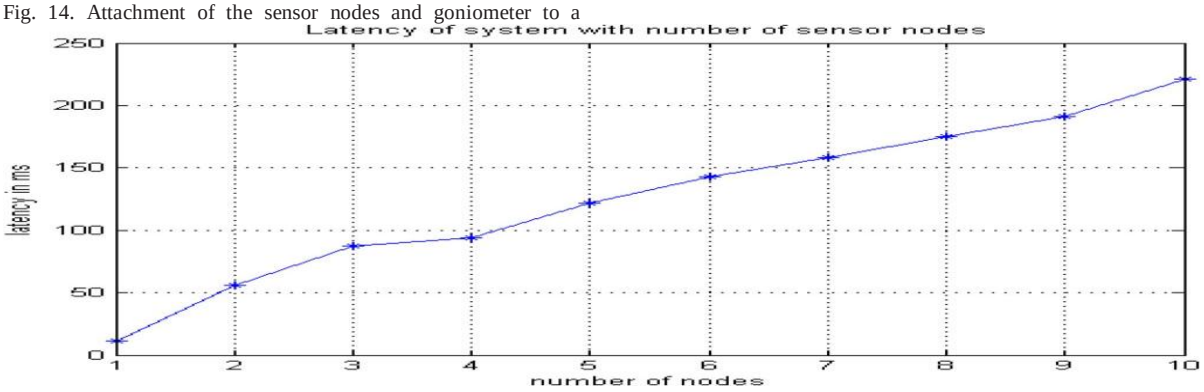

Fig.13.Latencyofasystemwithmultiplesensornodes.

TABLEIIBREAKDOWNOFPOWERCONSUMPTIONOFAT YPICALSENSORNODE

	Average Current Consumption	Average Power Consumption
PICLF2620 microcontroller	11uA	36.3uW
MMA7261QT 3-axis accelerometer	500uA	1.65mW
MRF24J40 RF transceiver	20mA	66mW
Entire sensor node	27mA	89mW

C. Power Consumption

A breakdown of a typical average power consumption of a sensor node in operation (at a sampling rate of 10 Hz) is given in Table II:

Using a 3.6-V rechargeable battery with a nominal capacity of 500 mAh, the sensor node should ideally last for about

18.5 h. As observed from Table II, the bulk of the power consumption comes from the RF transceiver, which consumes 20 mA of current in active mode. When placed in sleep mode, the transceiver consumes only 2 μA. As such, power management can further be improved by configuring the RF transceiver module to sleep when it is not transmitting. In this case, the average current consumption drops to 8.4 mA. This would prolong the battery life to about 59.5 h of continuous operation. Assuming a typical usage of 8 h per day, a single charge of the battery would allow it to be used for one week.

Fig. 15. Angle between the forearm and the upper limb obtained using the sensor nodes and a goniometer at different speeds.

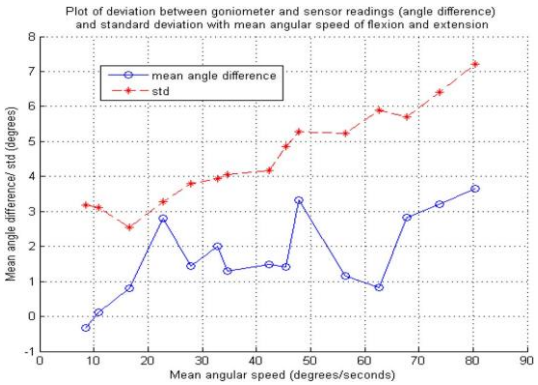

D. Comparison of the Proposed Approach With Goniometer Measurements

In Section VI-A, the accuracy of the sensor node for angle determination has been demonstrated. In this section, we benchmark the performance of the sensor nodes on an actual human arm with the readings from a goniometer probe (PS-2137 from PASCO). The goniometer consists of two metal arm links and a potentiometer. As the angle between the arm changes, the resistance of the potentiometer changes. The accuracy of the goniometer is $\pm 1^{\circ}$ when calibrated, with a resolution of 0.042° at a sampling rate of 500 Hz.

The attachment of the goniometer and the sensor node to the arm is shown in Fig. 14. The data logger for the goniometer is also shown on the left of Fig. 14. The sensor nodes are attached to the side of the goniometer so that measurements can be made with respect to the same reference frame for comparison. The subject is then asked to perform flexion and extension of his forearm for 100 s. The flexion and extension motion is then repeated 15 times. The subject is instructed to vary the speed of his motion in each time from the slowest in the first trial to the fastest in the last trial using a metronome as a reference. The mean error and standard deviation over the computed mean angular speed from these experiments are shown in Fig. 15. The offset in angle between the proposed system and the goniometer is found by taking the average of the difference in the readings at the maximum flexion and extension point of the forearm.

From Fig. 15, the mean difference in angle between the goniometer and the proposed system shows a linear increasing trend from close to 0° at a mean angular speed of 10 °/sto 3.5° at a mean angular speed of 80 °/s. The standard deviation also increases in a linear manner from 2.5° to 7° over the range of mean angular speeds. This result is similar to the experimental results in Section VI-A based on the rotary stage but is more pronounced when performed on the human arm. Several factors could have contributed to this effect. In this paper, we have assumed that the flexion and extension of the arm can be modeled as a rotating motion about a fixed axis and that the arm is a rigid body. In reality, there will be momentary changes in rotation axis due to muscles and joint movements during flexion and extension movements. Furthermore, the arm rotation may not be restricted in a 2-D plane.

VII. CONCLUSION

In this paper, an ambulatory and unrestrained measurement system based on a wearable wireless sensor network for tracking the human arm motion in the sagittal plane has been proposed. To study the performance of the prototype, controlled rotations of the prototype using a rotary stage show a mean error of only 0.52°. The developed system mounted on a human arm and evaluated with a goniometer shows a similar performance trend with a slight increase in error. These experiments demonstrate that the accuracy of the system is sufficiently good for the targeted rehabilitation application, where the angular velocity of the arm movement is less than 20°/s. Moreover, the latency of the system is less than 60 ms for a two-node network. Evaluation of the power consumption shows that the system can last for a week with a daily usage of 8 h.

As compared with other existing approaches, the new system is portable and easy to use. It allows the patients to be monitored without restraint, and rehabilitation can be carried out in a home environment instead of a specialized laboratory in the hospital. For future work, experiments conducted with stroke patients in collaboration with a hospital are being planned using the developed system. More tests can also be conducted to investigate the effect of RF interference from other patient monitoring devices and wireless systems.

REFERENCES

[1] H. Zhou and H. Hu, "Human motion tracking for rehabilitation—A survey," *Biomed. Signal Process. Control*, vol. 3, no. 1, pp. 1–18, Jan. 2008.

[2] J. M. Zheng, K. W. Chan, and I. Gibson, "Virtual reality," *IEEE Potentials*, vol. 17, no. 2, pp. 20–23, Apr. 1998.

[3] D. Jack, R. Boian, A. S. Merians, M. Tremaine, G. C. Burdea,S. V. Adamovich, M. Recce, and H. Poizner, "Virtual reality-enhanced stroke rehabilitation," *IEEE Trans. Neural Syst. Rehabil. Eng.*,vol.9, no. 3, pp. 308–318, Sep. 2001.

[4] D. Fitzgerald, J. Foody, D. Kelly, T. Ward, C. Markham, J. McDonald, and B. Caulfield, "Development of a wearable motion capture suit and virtual reality biofeedback system for the instruction and analysis of sports rehabilitation exercises," in *Proc. 29th Annu. Int. Conf. IEEE EMBS*, 2007, pp. 4870–4874.

[5] T. B. Moeslund, A. Hilton, and V. Krüger, "A survey of advances in vision-based human motion capture and analysis," *Comput. Vis. Image Underst.*, vol. 104, no. 2/3, pp. 90–126, Nov./Dec. 2006.

[6] G. Welch and E. Foxlin, "Motion tracking: No silver bullet, but a respectable arsenal," *IEEE Comput. Graph. Appl.*, vol. 22, no. 6, pp. 24–38, Nov./Dec. 2002.

[7] L. Wang, W. Hu, and T. Tan, "Recent developments in human motion analysis," *Pattern Recognit.*, vol. 36, no. 3, pp. 585–601, Mar. 2003.

[8] S. Miyazaki, "Long-term unrestrained measurement of stride length and walking velocity utilizing a piezoelectric gyroscope," *IEEE Trans. Biomed. Eng.*, vol. 44, no. 8, pp. 753–759, Aug. 1997.

[9] B. Kemp, A. J. M. W. Janssen, and B. van der Kamp, "Body position can be monitored in 3D using miniature accelerometers and earth-magnetic field sensors," *Electroencephalogr. Clin. Neurophysiol./ ElectromyographyMotorControl*, vol. 109, no. 6, pp. 484–488, Dec. 1998.

[10] D. Roetenberg, P. J. Slycke, and P. H. Veltink, "Ambulatory position and orientation tracking fusing magnetic and inertial sensing," *IEEE Trans. Biomed. Eng.*, vol. 54, no. 5, pp. 883–890, May 2007.

[11] R. Zhu and Z. Zhou, "A real-time articulated human motion tracking using tri-axis inertial/magnetic sensors package," *IEEE Trans. Neural Syst. Rehabil. Eng.*, vol. 12, no. 2, pp. 295–302, Jun. 2004.

[12] X. Yun and E. R. Bachmann, "Design, implementation, and experimental results of a quaternion-based Kalman filter for human body motion tracking," *IEEE Trans. Robot.*, vol. 22, no. 6, pp. 1216–1227, Dec. 2006.

[13] C. Jadhav and V. Krovi, "A low-cost framework for individualized interactive telerehabilitation," in *Proc. 26th Annu. Int. Conf. IEEE EMBS*, 2004, pp. 3297–3300.

[14] Y. Tao and H. Hu, "A novel sensing and data fusion system for 3-D arm motion tracking in telerehabilitation," *IEEE Trans. Instrum. Meas.*, vol. 57, no. 5, pp. 1029–1040, May 2008.

[15] G. M. Bertolotti, A. Cristiani, R. Gandolfi, and R. Lombardi, "A portable system for measuring human body movement," in *Proc. 9th EUROMICRO Conf. DSD*, 2006, pp. 569–576.

[16] S. Tanaka, K. Motoi, M. Nogawa, and K. Yamakoshi, "A new portable device for ambulatory monitoring of human posture and walking velocity using miniature accelerometers and gyroscope," in *Proc. 26th Annu. Int. Conf. IEEE EMBS*, 2004, vol. 3, pp. 2283–2286.

[17] T. Liu, Y. Inoue, and K. Shibata, "A wearable sensor system for human motion analysis and humanoid robot control," in *Proc. IEEE Int. Conf. ROBIO*, 2006, pp. 43–48.

[18] P. F. Binkley, "Predicting the potential of wearable technology," *IEEE Eng. Med. Biol. Mag.*, vol. 22, no. 3, pp.

23–27, May/Jun. 2003.

[19] T. Liu, Y. Inoue, K. Shibata, and R. Zheng, "Measurement of human lower limb orientations and ground reaction forces using wearable sensor systems," in *Proc. IEEE/ASME Int. Conf. Adv. Intell. Mechatronics*, 2007, pp. 1–6.

[20] H. Zhou, H. Hu, and N. Harris, "Application of wearable inertial sensors in stroke rehabilitation," in *Proc. 27th Annu. Int. Conf. IEEE EMBS*, 2005, pp. 6825–6828.

[21] D. Flowers and Y. Yang, AN1066—MiWi Wireless Networking Protocol Stack, 2007, [Online]. Available: http://ww1.microchip.com/downloads/ en/AppNotes/MiWi%20Application%20Note_AN1066.pdf

[22] K. S. Low, G. X. Lee, and T. Taher, "A wearable wireless sensor network for human limbs monitoring," in *Proc. IEEE I2MTC*, 2009, pp. 1332–1336

[23] J. Hamill and K. M. Knutzen, *Biomechanical Basis of Human Movement*, 3rd ed. Baltimore, MD: Lippincott Williams & Wilkins, 2009.

[24] B. Hingtgen, J. R. McGuire, M. Wang, and G. F. Harris, "An upper extremity kinematic model for evaluation of hemiparetic stroke," *J. Biomechanics*, vol. 39, no. 4, pp. 681–688, 2006.

[25] R. Beer, J. P. A. Dewald, M. L. Dawson, and W. Z. Rymer, "Targetdependent differences between free and constrained arm movements in chronic hemiparesis," *Exp. Brain Res.*, vol. 156, no. 4, pp. 458–470, Jun. 2004.

[26] G. Burdea and P. Coiffet, *Virtual Reality Technology*, 2nd ed. Hoboken, NJ: Wiley, 2003.

[27] C. V. C. Bouten, K. T. M. Koekkoek, M. Verduin, R. Kodde, and J. D. Janssen, "A triaxial accelerometer and portable data processing unit for the assessment of daily physical activity," *IEEE Trans. Biomed. Eng.*, vol. 44, no. 3, pp. 136–147, Mar. 1997.

Kay-Soon Low (M'88–SM'00) received the B.Eng. degree in electrical engineering from the National University of Singapore, Singapore, and the Ph.D. degree in electrical engineering from the University of New South Wales, Sydney, Australia.
He joined the School of Electrical and Electronic Engineering, Nanyang Technological University, Singapore, in 1994 as a Lecturer and subsequently became an Associate Professor. He is currently the Center Director of the Satellite Engineering Centre, Nanyang Technological University. He has served
as a consultant to many companies and has a number of granted patents on nonlinear circuits and UWB systems. His funded projects are in the field of UWB medical imaging, wireless sensor network, motion control system, pulse neural network, and satellite system.

Tawfiq Taher received the M.Sc. degree in computer control and automation from Nanyang Technological University, Singapore, in 2009.
After working with Automation and Control Solutions, Honeywell, he joined the Center for Environmental Sensing and Modeling, Singapore-MIT Alliance for Research and Technology, Singapore, as a Research Engineer. His current research interest includes multivehicle cooperative navigation and localization of autonomous underwater vehicle (AUV) for marine environment sensing, underwater acoustic
inter-AUV communication, and sonar-assisted real-time navigation of AUV using computer-aided detection and classification.